
A DENOISING FRAMEWORK FOR REAL-WORLD ULTRA-LOW DOSE LUNG CT IMAGES BASED ON AN IMAGE PURIFICATION STRATEGY

Guoliang Gong, Man Yu, Yu Zhang
Tianjin University of Science and Technology
gongguoliang@tust.edu.cn

Xianghong Meng, Xiaoliang Wang, Zhongwei Zhang
Department of Radiology, Tianjin Hospital

ABSTRACT

Ultra-low dose CT (uLDCT) significantly reduces radiation exposure but introduces severe noise and artifacts. It also leads to substantial spatial misalignment between uLDCT and normal dose CT (NDCT) image pairs. This poses challenges for directly applying existing denoising networks trained on synthetic noise or aligned data. To address this core challenge in uLDCT denoising, this paper proposes an innovative denoising framework based on an Image Purification (IP) strategy. First, we construct a real clinical uLDCT lung dataset. Then, we propose an Image Purification strategy that generates structurally aligned uLDCT-NDCT image pairs, providing a high-quality data foundation for network training. Building upon this, we propose a Frequency-domain Flow Matching (FFM) model, which works synergistically with the IP strategy to excellently preserve the anatomical structure integrity of denoised images. Experiments on the real clinical dataset demonstrate that our IP strategy significantly enhances the performance of multiple mainstream denoising models on the uLDCT task. Notably, our proposed FFM model combined with the IP strategy achieves state-of-the-art (SOTA) results in anatomical structure preservation. This study provides an effective solution to the data mismatch problem in real-world uLDCT denoising. Code and dataset are available at <https://github.com/MonkeyDadLufy/flow-matching>.

1 Introduction

Computed Tomography (CT) is a crucial diagnostic tool in clinical practice [1] [2]. During the COVID-19 pandemic, the frequency of CT examinations increased significantly, underscoring its value for crisis management [3] [4]. However, cumulative radiation dose from regular screenings may increase cancer risk, especially for pregnant women and children. Studies like the National Lung Screening Trial have shown a 20% reduction in lung cancer mortality among participants screened with low-dose CT (LDCT) [5]. Ultra-low dose CT can be achieved by reducing tube current or voltage. However, reducing the dose to ultra-low dose CT (uLDCT) levels, such as 2% of the original dose, causes a sharp decline in the signal-to-noise ratio. The resulting noise and artifacts far exceed those in conventional LDCT [6], severely impacting diagnosis (Fig.1(a)).

Although deep learning has advanced LDCT denoising [7] [8] [9], most methods rely on simulated LDCT-NDCT paired data or assume spatial alignment [10] [11]. For the more challenging uLDCT scenario, existing methods face two major bottlenecks. First, the complex noise and non-ideal physical effects in uLDCT are difficult to simulate using simple Poisson noise models. Second, the extremely low signal-to-noise ratio means that slight patient motion (e.g., breathing, heartbeat) between the uLDCT and NDCT scans leads to severe spatial misalignment (Fig. 1(b)). Directly training networks with such misaligned data pairs causes models to learn incorrect mappings, resulting in anatomical structure distortion in the denoised output (Fig.1(d)). This failure to preserve all anatomical structures from the input uLDCT image can directly affect diagnostic accuracy and is a major obstacle to the clinical application of uLDCT denoising techniques.

Recent work [12] attempted to alleviate misalignment by filtering image patches. However, on extremely noisy uLDCT data, this method filters out excessive data, leading to insufficient training (Fig.1(e)). Therefore, developing a method

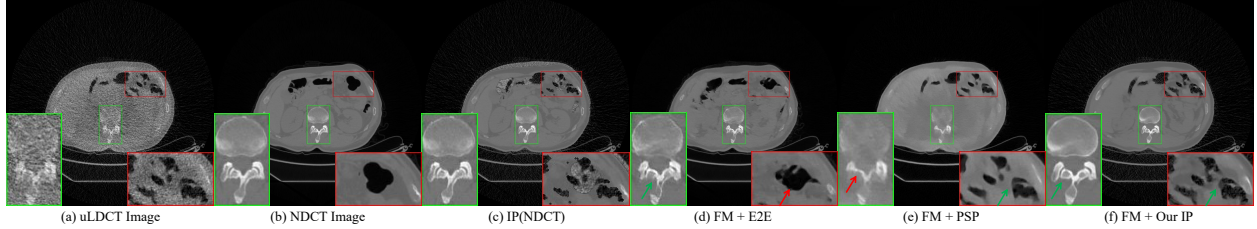


Figure 1: Motivation for the Image Purification (IP) Strategy. **(a)** Low-dose CT (LDCT) image with significant noise, affecting the clarity of tissue structures. **(b)** Normal-dose CT (NDCT) image corresponding to (a). The black area in the zoomed box shows the morphology of the anatomical structure. **(c)** Image after applying the IP strategy to the NDCT image, used as the label during testing. **(d)** Denoising result of (a) by end-to-end trained Flow Matching (FM [13]). **(e)** Denoising result of (a) by Flow Matching [13] trained with the PSP strategy [12]. **(f)** Denoising result of (a) by Flow Matching [13] trained with our IP strategy. Red arrows in (d) to (f) indicate inconsistent structures, green arrows indicate consistent structures.

that effectively overcomes the inherent spatial misalignment in real uLDCT-NDCT data pairs is a key challenge for enabling the clinical translation of uLDCT denoising. To address this issue, this paper proposes a systematic denoising framework, whose core is the Image Purification (IP) strategy. This strategy operates at the image level, effectively correcting structural misalignment between uLDCT and NDCT images (Fig.1(f)) and generating high-quality training data. Based on the data corrected by the IP strategy, we further propose a Frequency-domain Flow Matching (FFM) model to achieve superior structure-preserving denoising. The main contributions of this paper are as follows:

- Constructed a real clinical uLDCT lung dataset to provide a foundation for research.
- Proposed an innovative Image Purification (IP) strategy that effectively addresses the spatial misalignment problem in real uLDCT-NDCT data pairs.
- Proposed a Frequency-domain Flow Matching (FFM) model, which, combined with the IP strategy, achieves SOTA performance on uLDCT denoising.

The remainder of this paper is organized as follows. Section 2 introduces related work. Section 3 presents our proposed denoising framework. Experiments in Section 4 show that our IP strategy quantitatively and qualitatively enhances seven LDCT denoising networks, and our FFM model achieves SOTA results in contour preservation. Conclusions are summarized in Section 5.

2 RELATED WORK

This section reviews closely related work, including LDCT image denoising methods in Section 2.1 and methods addressing data misalignment in Section 2.2.

2.1 Low-Dose CT Image Denoising Networks

Most current CT denoising networks are designed for conventional LDCT scenarios. These methods can be broadly divided into two categories: one aims to remove noise n from the noisy LDCT image $y = x + n$ to obtain the target NDCT image x ; the other models the mapping relationship $f(\cdot)$ from the noisy LDCT image $y = f(x)$ to obtain the NDCT image x .

In the first category, REDCNN [14] employs a U-Net architecture and has achieved good results. EDCNN [15] introduces an edge enhancement module to improve contour preservation in the decoded denoised image. DUGAN [16] utilizes a U-Net-based discriminator to learn global and local differences between denoised and normal-dose images in both image and gradient domains, with the gradient domain design enhancing edges in denoised CT images. MMCA [17] adopts a Vision Transformer (ViT) macro-architecture and uses a Sobel operator to enhance edge information. These models perform well on general LDCT denoising tasks but struggle to recover fine details in the more challenging uLDCT task. Furthermore, although these models intentionally enhance contour preservation in their design, the "misalignment" in paired training data prevents the denoised results from fully preserving the original anatomical structures, affecting diagnostic accuracy.

In the second category, Cold Diffusion [18] extends traditional diffusion models by modifying the noise term in the denoising formula of DDPM [19] to arbitrary image types, transforming diffusion models into mapping functions

between any two distributions. CoreDiff [20] improves the noise addition formula of Cold Diffusion [18] by using an error modulation restoration network to correct sampling errors. Flow Matching [13] defines the conditional probability path for diffusion models using Optimal Transport (OT) displacement interpolation and employs numerical ODE solvers for fast sample generation. Resshift [21] uses OT displacement extrapolation to define the conditional probability path for Latent Diffusion Models [22], further reducing sampling steps. Networks based on diffusion models establish mapping relationships between two distributions through their noise addition formulas and can recover texture details in LDCT. However, the problem of structural distortion due to "misalignment" in paired training data persists.

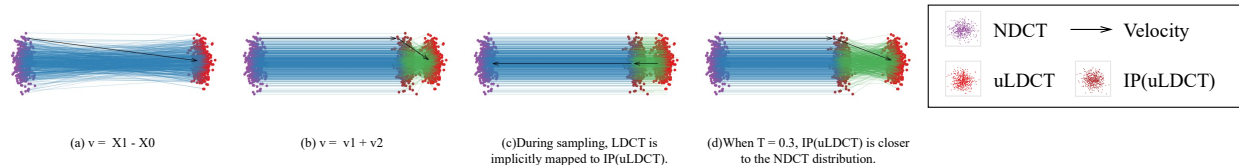


Figure 2: Concept of the Image Purification (IP) Strategy. **(a)** Mapping relationship of input data $(X_0, X_1) \sim (NDCT, uLDCT)$. Structural misalignment between X_0 and X_1 leads to intersecting trajectories. **(b)** By establishing a new distribution $X_1' \sim IP(uLDCT)$, decompose v into structure-consistent v_1 and texture-consistent v_2 . Use v_1 as the training data for the model. **(c)** During inference, X_1 is implicitly mapped from uLDCT to IP(uLDCT), and then reaches NDCT via the trained velocity field. **(d)** Parameter T influences the magnitude of v_1 .

2.2 Methods for Addressing Data Misalignment

Spatial misalignment between uLDCT and NDCT images creates numerous intersections in the mapping paths. These intersections make sampling difficult for networks; path crossing is a typical issue in flow matching models [13], as illustrated in Fig.2a. Rectified Flow [23] trains models with misaligned data pairs by simulating paths through filtering. However, this method merely establishes a mapping relationship from uLDCT to NDCT but fails to ensure that this mapping is "structure-preserving." During the training process, the model is not explicitly required to retain the anatomical structure of the input uLDCT images, which may consequently lead to distortion of the tissue architecture in the denoised output.

A common solution for data misalignment is to add Poisson noise to the sinogram of NDCT images to simulate LDCT [10] [11]. However, the significant gap between simulated and real LDCT noise prevents this method from being applied clinically. Work [24] proposed an LDCT image synthesis method based on Generative Adversarial Networks (GANs) and noise encoding transfer learning. Due to the complex degradation in uLDCT involving signal loss, complex artifacts, and structural damage, this method cannot effectively synthesize uLDCT images.

Another approach uses self-supervised methods, requiring only LDCT or NDCT data. N2N [25] employs a self-supervised noise2noise model and a noisy-as-clean strategy, adding noise multiple times to LDCT images and using singly and doubly corrupted images as substitutes for NDCT-LDCT image pairs to train the network, using only LDCT data. IPDM [26] iterates part of a full diffusion model to reduce computation time and is trained using only NDCT data. Self-supervised methods often assume noise is independent of the image with zero mean, which deviates from the reality that complex noise in real-world uLDCT images is strongly correlated with anatomical structures. Consequently, self-supervised denoising struggles to correctly remove complex noise from real uLDCT images.

To alleviate data misalignment, work [12] proposed a patch-level filtering strategy. However, this strategy faces significant challenges with our uLDCT lung data. The extreme noise and poor structural visibility in uLDCT images lead to a high proportion of patches being judged as "dissimilar," resulting in severely insufficient training data and ultimately poor denoising performance (Fig.1e). This highlights the need for a new, more robust data alignment solution specifically for the extreme scenario of uLDCT.

3 PROPOSED METHOD

Section 3.1 describes the specific procedure of our IP strategy. Section 3.2 outlines the model training and sampling process.

3.1 Image Purification Strategy

Our Image Purification (IP) strategy aims to resolve spatial misalignment between uLDCT and NDCT images. Its core idea is illustrated in Fig.2. From a probabilistic modeling perspective, data misalignment causes numerous

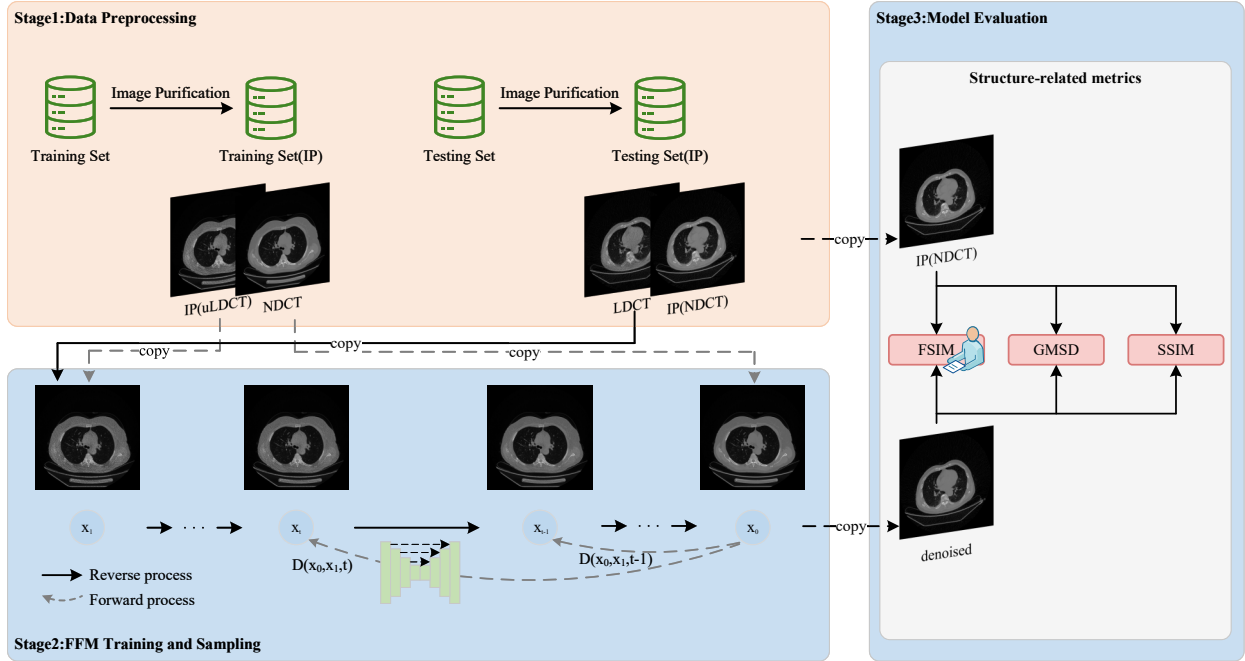


Figure 3: Overall Framework

intersections in the mapping paths from the uLDCT distribution to the NDCT distribution (Fig.2(a)), making the learning process for denoising models difficult and unstable. The core of the IP strategy is to construct an intermediate distribution—IP(uLDCT)—during the training phase. This distribution is structurally aligned with the NDCT distribution, thereby forming a more direct and easier-to-learn mapping in the probability path (Fig. 2(b)). During inference, the input uLDCT is implicitly mapped to the IP(uLDCT) distribution and then transformed to the NDCT distribution via the trained model (Fig.2(c)).

To quantify the "path straightening" effect of the IP strategy, we define a "crossover rate" to measure the severity of path intersections in the dataset. As shown in Fig.4, applying the IP strategy significantly reduces the dataset's crossover rate by a factor of 2 to 6 across different similarity thresholds, theoretically demonstrating that the IP strategy provides a superior data foundation for model training.

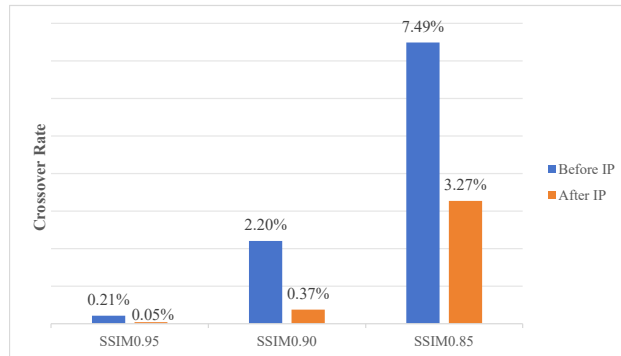


Figure 4: Effect of the Image Purification (IP) Strategy on Straightening Network Paths. We define the crossover rate as the proportion of samples with intersecting paths in the dataset. SSIM0.95, SSIM0.90, SSIM0.85 represent the cases where the similarity at the crossover point is $\geq 0.95, 0.90, 0.85$, respectively, among the samples with crossovers.

Our Image Purification (IP) strategy consists of five steps: Edge Extraction Binarization, Common Mask Calculation, Image Purification, Training Data Selection, and Label Selection.

Edge Extraction Binarization. This step uses Otsu’s Method [27] for adaptive binarization to compute binary masks for uLDCT and NDCT. This method separates the image’s contours and textures, outputting 1 for contour regions and 0 for texture regions.

Common Mask Calculation. In this step, we compute the common mask from the binary masks M_L and M_N obtained in the previous step. The common mask CM is derived by comparing M_L and M_N . For any pixel location x , if the binary value in either mask is 1 (indicating contour information), the value in the common mask at x is set to 1; otherwise, it is set to 0.

$$CM(x) = (M_L(x) \parallel M_N(x)) \quad (1)$$

In Fig.2b,

$$v_1 = X_1' - X_0 \quad (2)$$

$$v_2 = X_1 - X_1' \quad (3)$$

Substituting Equation 6 yields:

$$v_1 = (J - CM) \cdot v \quad (4)$$

$$v_2 = CM \cdot v \quad (5)$$

Here, J is an all-ones matrix, v represents the residual from NDCT to uLDCT, $J - CM$ and CM decompose the velocity v based on texture and contour components, respectively. The resulting v_1 exhibits texture change while preserving structure, and v_2 exhibits structure change while preserving texture.

Image Purification. We further propose:

$$LDCT_{IP} = (J - CM) \cdot LDCT + CM \cdot NDCT \quad (6)$$

$$NDCT_{IP} = (J - CM) \cdot NDCT + CM \cdot LDCT \quad (7)$$

$$LDCT_{IP} = (J - CM) \cdot [(1 - T) \cdot LDCT + T \cdot NDCT] + CM \cdot NDCT \quad (8)$$

Substituting the CM from the previous step into Equations 6 and 7 yields the purified uLDCT and NDCT. CM can be viewed as the anatomical contour weight, and $J - CM$ as the texture weight. The IP(uLDCT) obtained via Equation 6 possesses the anatomical contours of NDCT while retaining the texture of uLDCT. Similarly, the IP(NDCT) obtained via Equation 7 possesses the anatomical contours of uLDCT and the texture of NDCT. Equation 8 is further proposed to more finely control the amount of NDCT texture incorporated into uLDCT after the IP operation via parameter T . As shown in Fig.2(d), parameter T controls the distance from the constructed IP(uLDCT) distribution to the NDCT distribution. When $T = 0$, Equation 8 equals Equation 6, and IP(uLDCT) is farthest from the NDCT distribution. When $T = 1$, IP(uLDCT) = NDCT, and the distributions completely overlap. Equation 8 is used in the ablation study to validate the effect of T .

Training Data Selection. After applying the IP strategy, we obtained four sets of data of the same quantity: uLDCT, NDCT, IP(uLDCT), and IP(NDCT). Among them, uLDCT and IP(NDCT) share the same anatomical contours, and

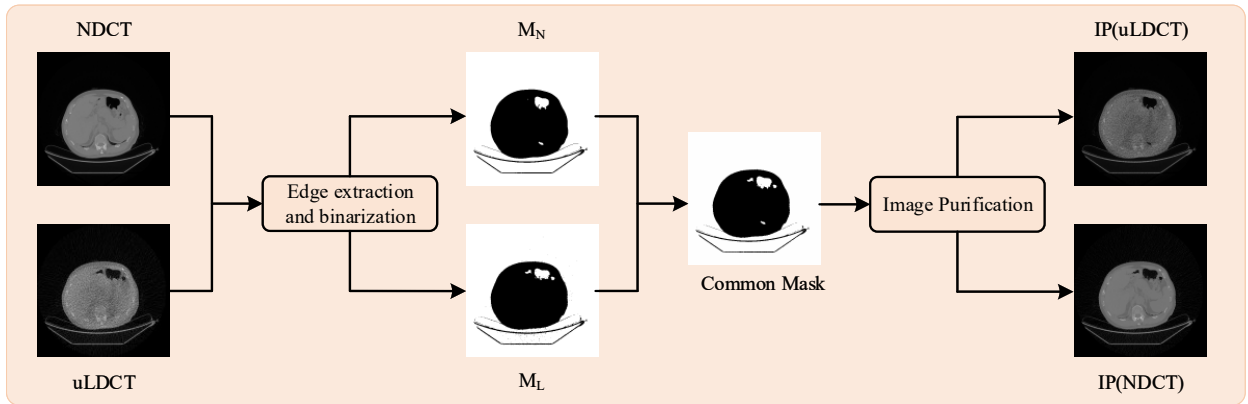


Figure 5: Proposed Image Purification (IP) Strategy.

NDCT and IP(uLDCT) share the same anatomical contours. Therefore, three data combinations can serve as the network training set:

1. NDCT & IP(uLDCT)
2. uLDCT & IP(NDCT)
3. NDCT & IP(uLDCT) and uLDCT & IP(NDCT) combined.

The ablation study section discusses the impact of these three combinations in detail. Unless otherwise specified, the experiments in this paper use Combination 1.

Label Selection. As mentioned, uLDCT and NDCT have different anatomical contours, making it suboptimal to use NDCT directly as the denoising target for uLDCT. For a uLDCT denoising network, given a uLDCT input, we want the output image to restore more texture details while preserving the anatomical contours of the input uLDCT image. The IP(NDCT) obtained via Equation 7 possesses both the anatomical contours of the uLDCT image and the texture of NDCT, perfectly meeting the requirements for uLDCT denoising. Therefore, in our framework, we use IP(NDCT) as the target label for uLDCT denoising.

3.2 FFM Model

We use Flow Matching [13] as the baseline and migrate its main network from the image domain to the frequency domain to further enhance its contour preservation capability.

As shown in Fig.3, the proposed diffusion model includes a forward process and a reverse process. In the forward process, Equation 9 is used to obtain the image x_t at any time t , and x_t and t are used to train the neural network. In the reverse process, a numerical method iteratively solves for the image at the next time step until x_0 is obtained.

A U-Net is adopted as the backbone. For the input of each layer in the U-Net, as shown in Fig.6, we use a 2D Fast Fourier Transform (FFT) to transform spatial information into the frequency domain. Frequency domain information consists of two components: magnitude and phase. We apply two separate 1×1 convolutions to the magnitude and phase components to preserve original structural information. Subsequently, an Inverse Fast Fourier Transform (IFFT) is used to transform the features back to the spatial domain [28].

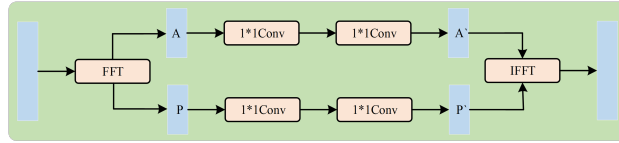


Figure 6: Frequency Domain Module of FFM.

The following is the one-step noise addition formula for FFM in Figure 3:

$$X_t = D(X_0, X_1, t) = t \cdot X_1 + (1 - t) \cdot X_0 \quad (9)$$

The pseudocode for the training and sampling processes of FFM is presented in Algorithm 1 and Algorithm 2, respectively.

Algorithm 1 Training for FFM

- 1: **Input:** Paired NDCT and IP(uLDCT) image sets, $I = \{(x_0, x_1)_i\}_{i=1}^N$, time range $[0, 1]$
 - 2: **Output:** Trained R_θ
 - 3: Initialization: Randomly initialize R_θ
 - 4: **repeat**
 - 5: Sample $(x_0, x_1) \sim I$
 - 6: Sample $t \sim \text{Uniform}(0, 1)$
 - 7: Calculate x_t by linear interpolation: $x_t = t \cdot x_1 + (1 - t) \cdot x_0$
 - 8: Calculate v_t by: $v_t = x_1 - x_0$
 - 9: Calculate \hat{v}_t by: $\hat{v}_t = R_\theta(x_t, t)$
 - 10: Update θ by minimize $\mathcal{L}(\theta) = \mathbb{E}_{t, x_0, x_1} \|\hat{v}_t - v_t\|_2^2$
 - 11: **until** converged
-

Algorithm 2 Sampling for FFM (Euler Method)

```
1: Input: A test uLDCT image  $x_1$ , number of steps  $T$ , trained model  $R_\theta$ 
2: Output: Denoised image  $x_0$ 
3: Load the trained  $R_\theta$ 
4: Set  $x = x_1$ 
5: Set  $\Delta t = 1/T$ 
6: for  $t = 1, 1 - \Delta t, \dots, 0$  do
7:   Calculate  $\hat{v}$  by:  $\hat{v} = R_\theta(x, t)$ 
8:   Update:  $x = x - \Delta t \cdot \hat{v}$ 
9: end for
10:  $x_0 = x$ 
11: return  $x_0$ 
```

4 EXPERIMENTS

This section first describes the dataset in 4.1 and introduces the experimental setup in 4.2. Then, we evaluate different methods on our real-world patient lung ultra-low dose dataset in 4.3. Finally, we conduct ablation studies in 4.4.

4.1 Our Real-World Datasets

We conduct experiments on a collected real-world dataset. For our patient dataset, a total of 4310 uLDCT and NDCT image pairs were captured from 6 patients. We randomly selected 3017 pairs for training, 646 for validation, and 647 for testing. For each CT scan, we recorded the tube voltage and current values. Under normal dose, the values were 120kV and 250mA, respectively. Under low dose, they were reduced to 80kV and 10mA, respectively. This reduction introduces significant noise and artifacts. We observed that the radiation exposure for the LDCT scans is approximately 2% of that for the NDCT scans, placing it in the ultra-low dose category. For each uLDCT or NDCT image from the training set, we generate new uLDCT and NDCT images using the IP strategy. The generated uLDCT (IP(uLDCT)) and the original NDCT are used to train the denoising network, while the generated NDCT (IP(NDCT)) is used to evaluate the denoising network’s performance. This image-level purification approach does not reduce the dataset size and is suitable for both image-based and patch-based training networks.

4.2 Experimental Setup

Implementation Details. For networks providing training code, default settings were used. For networks without provided training code, the Adam optimizer [29] was uniformly used with an initial learning rate of 10^{-4} and a batch size of 2. We trained the denoising networks on an NVIDIA RTX 4090 GPU. For the proposed FFM model, the number of epochs was set to 200, the Euler method was used for sampling, and the number of time steps was set to 10.

Evaluation Metrics. Traditional LDCT denoising networks use three evaluation metrics: SSIM, PSNR, and RMSE. Building on this, we introduce four additional metrics: FSIM, GMSD, VIF, and NQM. Previous research has shown that FSIM, VIF, and NQM align more closely with radiologists’ subjective assessments [30]. We group these seven metrics into two categories: The first group includes FSIM, GMSD, and SSIM, used to assess the model’s ability to recover anatomical contours. The second group includes VIF, NQM, PSNR, and RMSE, used to evaluate the model’s ability to recover texture details. In experiments validating the effectiveness of the IP strategy, we focus on contour recovery and use FSIM, GMSD, and SSIM. To investigate the impact of parameter T on both contour and texture recovery, we use all seven metrics mentioned above.

4.3 Comparison on Real-World uLDCT Images

We compare the performance of seven LDCT image denoising networks trained with and without our IP strategy on our real-world Patient dataset.

4.3.1 Comparison Methods

1. We compare the structural similarity of LDCT images with and without our strategy to NDCT.
2. We compare 5 LDCT image denoising networks (CoreDiff [20], REDCNN [14], EDCNN [15], DuGAN [16], MMCA [17]) and 2 general image denoising networks (Flow Matching [13], Cold Diffusion [18]), trained on our real-world patient lung dataset with and without our strategy.

Table 1: Quantitative Results (Mean \pm Standard Deviation) of Different Algorithms on the Real Patient Lung Dataset. Improvement rates over the baseline method in the previous column are shown as percentages. **Red**, **blue**, and underlined text indicate the best, second-best, and third-best results, respectively.

Method		FSIM \uparrow		GMSD \downarrow		SSIM \uparrow
uLDCT		0.5020 \pm 0.0717		0.7196 \pm 0.0130		0.4788 \pm 0.1197
uLDCT + IP	57%	0.7889 \pm 0.0871	18%	0.5870 \pm 0.0982	63%	0.7814 \pm 0.1118
flow matching [13]		0.8556 \pm 0.0269		0.5132 \pm 0.0307		0.8740 \pm 0.0651
flow matching [13] + IP	8%	<u>0.9262\pm0.0359</u>	28%	0.3691\pm0.0627	5%	0.9160\pm0.0639
CoreDiff [20]		0.8309 \pm 0.0500		0.6977 \pm 0.0340		<u>0.9134\pm0.0408</u>
CoreDiff [20] + IP	8%	0.8958 \pm 0.0632	25%	0.5249 \pm 0.1046	-1%	0.9057 \pm 0.0737
Cold Diffusion [18]		0.8706 \pm 0.0219		0.5205 \pm 0.0482		0.8970 \pm 0.0547
Cold Diffusion [18] + IP	7%	<u>0.9308\pm0.0302</u>	27%	<u>0.3788\pm0.0551</u>	2%	0.9120 \pm 0.0577
REDCNN [14]		0.8047 \pm 0.0339		0.6941 \pm 0.0728		0.8674 \pm 0.0472
REDCNN [14] + IP	12%	0.8985 \pm 0.0538	39%	0.4201 \pm 0.0896	3%	0.8936 \pm 0.0744
EDCNN [15]		0.7561 \pm 0.0382		0.6625 \pm 0.0464		0.8192 \pm 0.0373
EDCNN [15] + IP	16%	0.8782 \pm 0.0515	30%	0.4615 \pm 0.0790	6%	0.8706 \pm 0.0723
DuGAN [16]		0.7964 \pm 0.0361		0.5210 \pm 0.0340		0.8369 \pm 0.0559
DuGAN [16] + IP	14%	0.9107 \pm 0.0396	25%	0.3931 \pm 0.0627	6%	0.8900 \pm 0.0761
MMCA [17]		0.6478 \pm 0.0325		0.6026 \pm 0.0533		0.8025 \pm 0.0607
MMCA [17] + IP	38%	0.8935 \pm 0.0505	28%	0.4317 \pm 0.0839	11%	0.8884 \pm 0.0781
N2N [25]		0.5406 \pm 0.0902		0.7215 \pm 0.0278		0.5484 \pm 0.1546
IPDM [26]		0.5205 \pm 0.0656		0.7346 \pm 0.0176		0.5316 \pm 0.1264
Resshift [21]		0.8073 \pm 0.0206		0.6864 \pm 0.0313		0.7538 \pm 0.0290
FFM(ours) + IP		0.9342\pm0.0341		0.3708\pm0.0665		0.9230\pm0.0625

3. We compare 2 LDCT image denoising networks (unsupervised method IPDM [26], self-supervised method N2N [25] and 1 general image denoising network (supervised method Resshift [21])).
4. We propose the Frequency-domain Flow Matching (FFM) model, trained on our real-world patient lung dataset using our strategy.

4.3.2 Quantitative Results

The results in Table 1 demonstrate the universality of our IP strategy in enhancing the performance of various LDCT denoising models. Compared to their baselines, all methods show consistent improvement in contour preservation metrics (FSIM, GMSD, SSIM) when combined with the IP strategy. Notably, simpler models like REDCNN [14] and EDCNN [15] exhibit larger improvements. This phenomenon suggests that for the uLDCT denoising task, addressing the quality of training data (i.e., structural alignment) is a fundamental prerequisite for model performance, potentially even more critical than the complexity of the model architecture itself. Powerful generative models like Flow Matching [13] and Cold Diffusion [18] also break through performance bottlenecks with the assistance of the IP strategy, achieving higher denoising quality.

The performance differences among models also reflect the challenges of uLDCT denoising: Unsupervised (IPDM [26]) and self-supervised (N2N [25]) methods perform poorly due to the lack of clear supervision signals; the latent diffusion model (Resshift [21]), operating in a low-dimensional latent space, inevitably loses some high-frequency detail information during encoding and decoding, which may limit its performance in uLDCT tasks requiring high-precision structural recovery. Our proposed FFM model, empowered by the IP strategy, achieves the best overall performance, validating the effectiveness of our framework.

4.3.3 Visual Quality

As shown in Fig.7(c) and Fig.7(d), for anatomical contours present in uLDCT but absent in NDCT, our IP strategy fills these contours in uLDCT to align it with NDCT. Similarly, it creates new contours in NDCT to align it with uLDCT. Fig.7(e)-h) show results from models trained without our IP-corrected image pairs: Flow Matching [13], Cold Diffusion [18], and MMCA [17] fill in the contours present in uLDCT; CoreDiff [20] and REDCNN [14] cause partial deformation of the contours; EDCNN [15] and DuGAN [16] blur the contours. In summary, these methods alter the original anatomical contours of the uLDCT input. Fig.7(i)-(r) show results from models trained with our IP-corrected

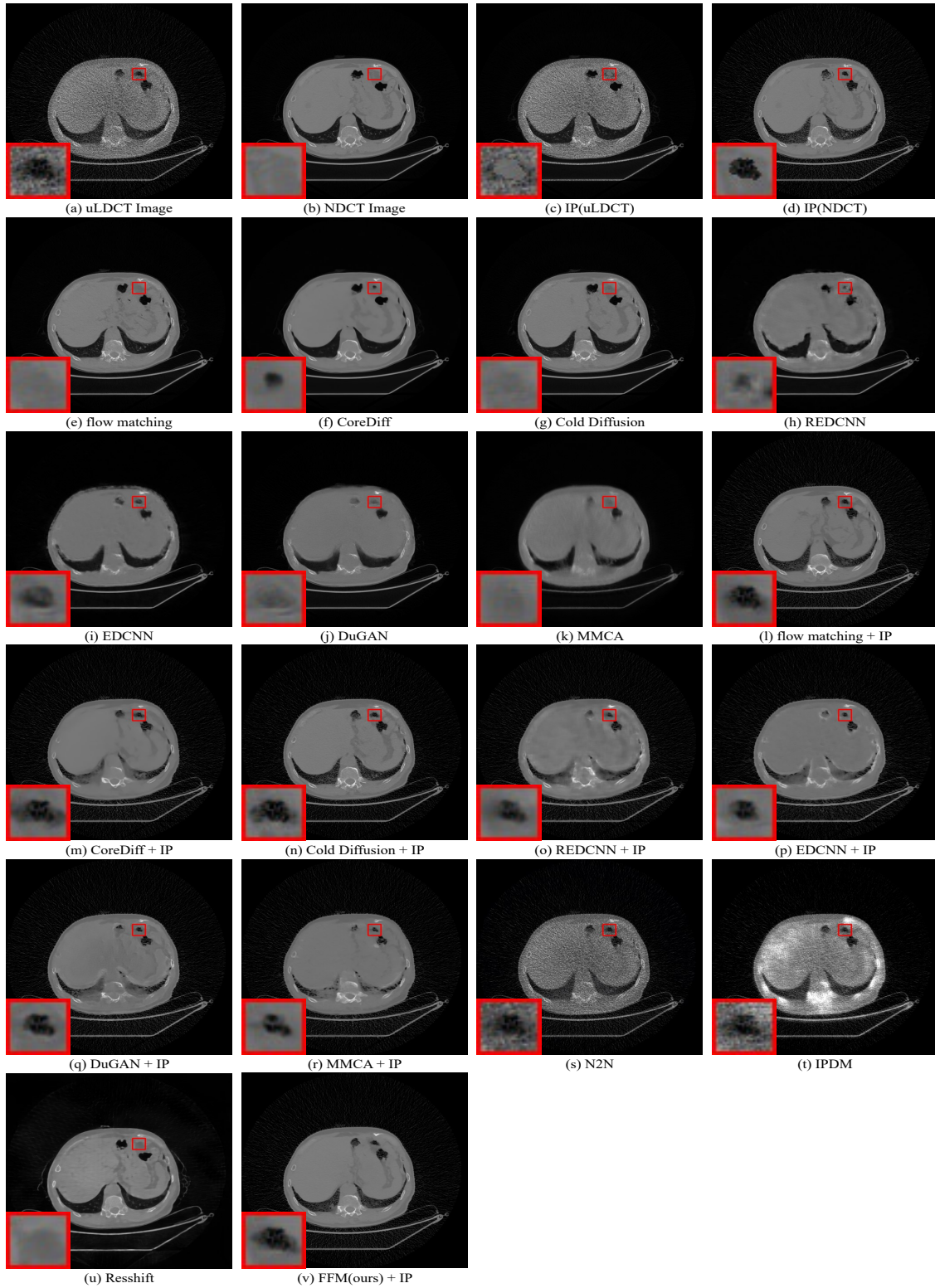


Figure 7: Comparison of Visual Quality by Different Denoising Methods on One uLDCT Image from Our Patient Dataset.

image pairs: these methods successfully preserve the anatomical contours of the input uLDCT. In Fig.7(s), N2N [25] shows little denoising capability. In Fig.7(t), IPDM [26] produces blurry results. In Fig. 7(u), Resshift [21], similar to Fig.7(o)-(r), exhibits noticeable streaking artifacts. Our FFM model in Fig.7(v), compared to Fig.7(l)-(n), preserves more complete anatomical contour information from the uLDCT input. More visual quality comparisons are provided in the supplementary file.

4.4 Ablation Study

Here, we evaluate:

1. How does parameter T affect the performance of uLDCT denoising networks?
2. How do different data pairs affect the performance?
3. Performing uLDCT denoising in different domains.

1.Impact of Parameter T.The value of T controls the amount of NDCT texture incorporated into the constructed IP(uLDCT) image. Therefore, while keeping the anatomical contour component unchanged, we vary T and train the FM model on the patient dataset. Results are shown in Table 2. It can be observed that when T=0.0, FM achieves the best SSIM result. When T=0.1, FM achieves the best results for FSIM, VIF, NQM, PSNR, and RMSE. This indicates that appropriately adding NDCT texture to the constructed IP(uLDCT) image helps improve the performance of uLDCT denoising networks.

Table 2: Results of Training FM [13] on Patient Data with Different T Values.

T	FSIM \uparrow	GMSD \downarrow	SSIM \uparrow	VIF \uparrow	NQM \uparrow	PSNR \uparrow	RMSE \downarrow
0.0	0.9294	0.3663	0.9183	0.8063	19.83	30.88	8.0
0.1	0.9305	0.3735	0.9170	0.8603	20.76	31.49	7.4
0.2	0.9269	0.3924	0.9099	0.7337	17.51	29.15	9.8
0.3	0.9277	0.3539	0.9062	0.7659	17.67	29.19	9.7
0.4	0.9252	0.3689	0.8936	0.7981	17.87	29.28	9.6
0.5	0.9180	0.3917	0.8827	0.7558	16.36	28.06	11.0

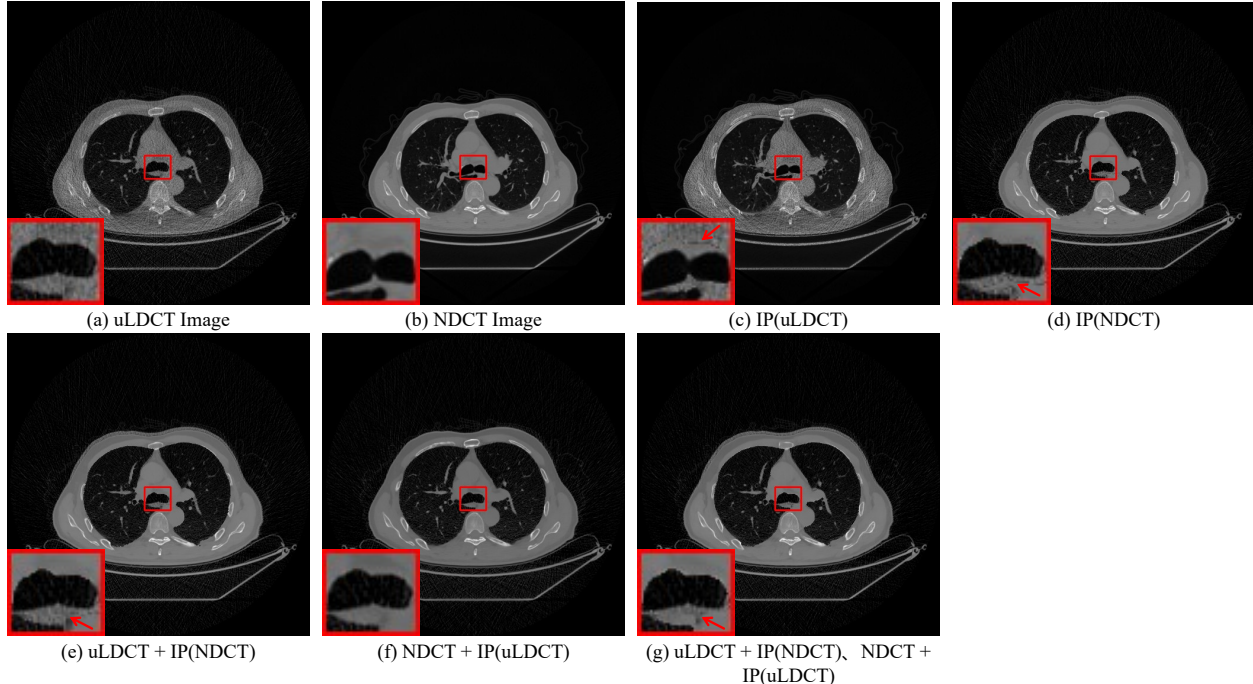


Figure 8: Comparison of Visual Quality by Different Training Data Pairs on One uLDCT Image from Our Patient Dataset. (a) to (d) are training data. (e) to (g) are sampling results using flow matching [13] under different training data, respectively. The red arrow indicates the overlapping trace of contours after using the IP strategy on the two images.

2. Impact of Different Training Data Pairs. Our IP strategy corrects both uLDCT and NDCT, leading to three training strategies: uLDCT & IP(NDCT) (Fig.8(e)), NDCT & IP(uLDCT) (Fig.8(f)), and a combination of both (Fig.8(g)). The IP strategy can create a granular effect at the edges where the anatomical contours of the two images overlap (red arrows in Fig.8(c), (d)). The choice of training data affects performance. The results in Fig.8(e) and Fig.8(g) show edge granularity similar to Fig.8(d), while Fig.8(f) does not. This is because both Fig.8(e) and Fig.8(g) use uLDCT and IP(NDCT), constructing a mapping from uLDCT to IP(NDCT). Consequently, the network samples from the IP(NDCT) distribution, which deviates from the true NDCT distribution.

3. Denoising in Different Domains. In the image domain, signal and noise are difficult to separate, limiting denoising network performance. We propose the FFM model operating in the frequency domain. Comparing FFM with its image-domain baseline (FM [13]), Table 2 shows that FFM outperforms FM [13] on 6 out of 7 metrics (except GMSD), indicating that denoising in the frequency domain can enhance performance.

Table 3: Results of Training FM [13] in Different Domains on the Patient Dataset.

Domain	FSIM \uparrow	GMSD \downarrow	SSIM \uparrow	VIF \uparrow	NQM \uparrow	PSNR \uparrow	RMSE \downarrow
Frequency	0.9342	0.3708	0.9230	0.9054	21.78	32.25	6.9
Image	0.9292	0.3587	0.9179	0.8964	21.37	31.85	7.1

5 CONCLUSION

This paper addresses the inherent spatial misalignment problem in real-world ultra-low dose CT (uLDCT) denoising by proposing a systematic solution based on an Image Purification (IP) strategy. Through the construction of a real clinical uLDCT dataset, an innovative IP data preprocessing method, and a Frequency-domain Flow Matching (FFM) model, we effectively mitigate the structural distortion in denoised images caused by data misalignment. Experiments

demonstrate that the IP strategy universally enhances the performance of existing denoising methods on uLDCT, while our FFM model achieves state-of-the-art structure preservation.

Limitations: The proposed method denoises the Region of Interest (ROI) but retains background noise. This is due to the implicit mapping of uLDCT to IP(uLDCT) during the sampling process. Eliminating this background noise is an important part of our future work. Our denoising framework aims to restore as much NDCT texture as possible while preserving the anatomical contours of the uLDCT image. Although the proposed method achieves competitive performance on the current dataset, denoising ultra-low dose CT at 2% of the normal dose radiation level remains a challenging task.

References

- [1] Atsuhiko Handa, Taiki Nozaki, Akari Makidono, Tetsuhiko Okabe, Yuka Morita, Kazutoshi Fujita, Masaki Matsusako, Tatsuo Kono, Yasuyuki Kurihara, Daisuke Hasegawa, et al. Pediatric oncologic emergencies: clinical and imaging review for pediatricians. *Pediatrics International*, 61(2):122–139, 2019.
- [2] Jennifer L Goralski, Neil J Stewart, and Jason C Woods. Novel imaging techniques for cystic fibrosis lung disease. *Pediatric pulmonology*, 56:S40–S54, 2021.
- [3] Xingzhi Xie, Zheng Zhong, Wei Zhao, Chao Zheng, Fei Wang, and Jun Liu. Chest ct for typical coronavirus disease 2019 (covid-19) pneumonia: relationship to negative rt-pcr testing. *Radiology*, 296(2):E41–E45, 2020.
- [4] Tao Ai, Zhenlu Yang, Hongyan Hou, Chenao Zhan, Chong Chen, Wenzhi Lv, Qian Tao, Ziyong Sun, and Liming Xia. Correlation of chest ct and rt-pcr testing for coronavirus disease 2019 (covid-19) in china: a report of 1014 cases. *Radiology*, 296(2):E32–E40, 2020.
- [5] National Lung Screening Trial Research Team. Reduced lung-cancer mortality with low-dose computed tomographic screening. *New England Journal of Medicine*, 365(5):395–409, 2011.
- [6] Emilio Quaia, Elisa Baratella, Stefano Cernic, Arianna Lorusso, Federica Casagrande, Vincenzo Cioffi, and Maria Assunta Cova. Analysis of the impact of digital tomosynthesis on the radiological investigation of patients with suspected pulmonary lesions on chest radiography. *European radiology*, 22(9):1912–1922, 2012.
- [7] Simon LF Walsh, Lucio Calandriello, Mario Silva, and Nicola Sverzellati. Deep learning for classifying fibrotic lung disease on high-resolution computed tomography: a case-cohort study. *The Lancet Respiratory Medicine*, 6(11):837–845, 2018.
- [8] Philipp Tschandl, Noel Codella, Bengü Nisa Akay, Giuseppe Argenziano, Ralph P Braun, Horacio Cabo, David Gutman, Allan Halpern, Brian Helba, Rainer Hofmann-Wellenhof, et al. Comparison of the accuracy of human readers versus machine-learning algorithms for pigmented skin lesion classification: an open, web-based, international, diagnostic study. *The lancet oncology*, 20(7):938–947, 2019.
- [9] Zachi I Attia, Peter A Noseworthy, Francisco Lopez-Jimenez, Samuel J Asirvatham, Abhishek J Deshmukh, Bernard J Gersh, Rickey E Carter, Xiaoxi Yao, Alejandro A Rabinstein, Brad J Erickson, et al. An artificial intelligence-enabled ecg algorithm for the identification of patients with atrial fibrillation during sinus rhythm: a retrospective analysis of outcome prediction. *The Lancet*, 394(10201):861–867, 2019.
- [10] Cynthia H McCollough, Adam C Bartley, Rickey E Carter, Baiyu Chen, Tammy A Drees, Phillip Edwards, David R Holmes III, Alice E Huang, Farhana Khan, Shuai Leng, et al. Low-dose ct for the detection and classification of metastatic liver lesions: results of the 2016 low dose ct grand challenge. *Medical physics*, 44(10):e339–e352, 2017.
- [11] KA Saneera Hemantha Kulathilake, Nor Aniza Abdullah, Aznul Qalid Md Sabri, and Khin Wee Lai. A review on deep learning approaches for low-dose computed tomography restoration. *Complex & Intelligent Systems*, 9(3):2713–2745, 2023.
- [12] Zeya Song, Liqi Xue, Jun Xu, Baoping Zhang, Chao Jin, Jian Yang, and Changliang Zou. Real-world low-dose ct image denoising by patch similarity purification. *IEEE Transactions on Image Processing*, 2024.
- [13] Yaron Lipman, Ricky TQ Chen, Heli Ben-Hamu, Maximilian Nickel, and Matt Le. Flow matching for generative modeling. *arXiv preprint arXiv:2210.02747*, 2022.
- [14] Hu Chen, Yi Zhang, Mannudeep K Kalra, Feng Lin, Yang Chen, Peixi Liao, Jiliu Zhou, and Ge Wang. Low-dose ct with a residual encoder-decoder convolutional neural network. *IEEE transactions on medical imaging*, 36(12):2524–2535, 2017.
- [15] Tengfei Liang, Yi Jin, Yidong Li, and Tao Wang. Edcnn: Edge enhancement-based densely connected network with compound loss for low-dose ct denoising. In *2020 15th IEEE International conference on signal processing (ICSP)*, volume 1, pages 193–198. IEEE, 2020.

- [16] Zhizhong Huang, Junping Zhang, Yi Zhang, and Hongming Shan. Du-gan: Generative adversarial networks with dual-domain u-net-based discriminators for low-dose ct denoising. *IEEE Transactions on Instrumentation and Measurement*, 71:1–12, 2021.
- [17] Jianfang Li, Li Wang, Shengxiang Wang, Yakang Li, and Fazhi Qi. Mmca: Multi-stage multi-order context aggregation framework for ldct denoising. *Applied Intelligence*, 55(7):1–14, 2025.
- [18] Arpit Bansal, Eitan Borgnia, Hong-Min Chu, Jie Li, Hamid Kazemi, Furong Huang, Micah Goldblum, Jonas Geiping, and Tom Goldstein. Cold diffusion: Inverting arbitrary image transforms without noise. *Advances in Neural Information Processing Systems*, 36:41259–41282, 2023.
- [19] Jonathan Ho, Ajay Jain, and Pieter Abbeel. Denoising diffusion probabilistic models. *Advances in neural information processing systems*, 33:6840–6851, 2020.
- [20] Qi Gao, Zilong Li, Junping Zhang, Yi Zhang, and Hongming Shan. Corediff: Contextual error-modulated generalized diffusion model for low-dose ct denoising and generalization. *IEEE Transactions on Medical Imaging*, 43(2):745–759, 2023.
- [21] Zongsheng Yue, Jianyi Wang, and Chen Change Loy. Efficient diffusion model for image restoration by residual shifting. *IEEE Transactions on Pattern Analysis and Machine Intelligence*, 2024.
- [22] Robin Rombach, Andreas Blattmann, Dominik Lorenz, Patrick Esser, and Björn Ommer. High-resolution image synthesis with latent diffusion models. In *Proceedings of the IEEE/CVF conference on computer vision and pattern recognition*, pages 10684–10695, 2022.
- [23] Xingchao Liu, Chengyue Gong, and Qiang Liu. Flow straight and fast: Learning to generate and transfer data with rectified flow. *arXiv preprint arXiv:2209.03003*, 2022.
- [24] Ming Li, Jiping Wang, Yang Chen, Yufei Tang, Zhongyi Wu, Yujin Qi, Haochuan Jiang, Jian Zheng, and Benjamin MW Tsui. Low-dose ct image synthesis for domain adaptation imaging using a generative adversarial network with noise encoding transfer learning. *IEEE transactions on medical imaging*, 42(9):2616–2630, 2023.
- [25] Yuting Zhu, Qiang He, Yudong Yao, and Yueyang Teng. Self-supervised noise2noise method utilizing corrupted images with a modular network for ldct denoising. *Pattern Recognition*, 161:111285, 2025.
- [26] Feiyang Liao, Yufei Tang, Qiang Du, Jiping Wang, Ming Li, and Jian Zheng. Domain progressive low-dose ct imaging using iterative partial diffusion model. *IEEE Transactions on Medical Imaging*, 2024.
- [27] Nobuyuki Otsu et al. A threshold selection method from gray-level histograms. *Automatica*, 11(285-296):23–27, 1975.
- [28] Kai Shang, Mingwen Shao, Chao Wang, Yuanshuo Cheng, and Shuigen Wang. Multi-domain multi-scale diffusion model for low-light image enhancement. In *Proceedings of the AAAI conference on artificial intelligence*, volume 38, pages 4722–4730, 2024.
- [29] Ilya Loshchilov, Frank Hutter, et al. Fixing weight decay regularization in adam. *arXiv preprint arXiv:1711.05101*, 5(5):5, 2017.
- [30] Allister Mason, James Rioux, Sharon E Clarke, Andreu Costa, Matthias Schmidt, Valerie Keough, Thien Huynh, and Steven Beyea. Comparison of objective image quality metrics to expert radiologists’ scoring of diagnostic quality of mr images. *IEEE transactions on medical imaging*, 39(4):1064–1072, 2019.